Numerical exploration of flow topology and vortex stability in a curved duct

S. F. Tsai[1,§] and Tony W. H. Sheu[2,*,†,‡]

[1]*Department of Marine Engineering, National Taiwan Ocean University, No. 2, Beining Road, Keelung, Taiwan 202, Republic of China*
[2]*Department of Engineering Science and Ocean Engineering, National Taiwan University, No. 1, Sec. 4, Roosevelt Road, Taipei, Taiwan 106, Republic of China*

SUMMARY

We performed incompressible flow simulation in a square duct with 90° bend and a curvature radius of 2.3 to extend our understanding of the vortical flow development in the bend. The solutions for the flow investigated at the Reynolds number of $Re = 790$ are obtained in a tri-quadratic element system, where velocities stagger the pressure working variable, using the streamline-upwind finite element model and the BiCGSTAB iterative solver. The simulated results reveal that centrifugal force convects the quickly moving fluid particles towards the outer wall. The axial velocity, as a result, shows twin peaks in the curved channel. At about $\theta = 66°$, the secondary flow shows three complex pairs of vortices. Also noteworthy is the formation of a downstream spiralling flow motion. To better elucidate the dominating three-dimensional flow nature, the topological study of limiting streamlines was undertaken. Insight into the longitudinal flow instability is gained by tracking the formation and diminishing of limiting cycles. Copyright © 2006 John Wiley & Sons, Ltd.

1. INTRODUCTION

Flows in curved ducts can be found in pumps, aircraft intakes, river bends, and cooling coils in heat exchangers. Their practical importance has motivated considerable research effort in the

---

*Correspondence to: Tony W. H. Sheu, Department of Engineering Science and Ocean Engineering, National Taiwan University, No. 1, Sec. 4, Roosevelt Road, Taipei, Taiwan 106, Republic of China.
†E-mail: twhsheu@ntu.edu.tw
‡Professor.
§Assistant Professor.

past. In curved ducts, centrifugal and viscous (Tollmien–Schlichting) instabilities may coexist and interact strongly [1]. The resulting non-linear interaction between these instabilities can cause the flow to evolve to exhibit turbulence at a higher Reynolds number. Advancing of knowledge about this three-dimensional curved flow is, thus, of fundamental importance.

One of the main flow characteristics in curved pipes or channels is the secondary flow, which was first reported by Eustice [2, 3] in curved pipes and could have a significant influence on the primary flow development in regions of prevailing centrifugal force. Later on, this experimentally observed phenomenon was analytically confirmed by Dean [4, 5]. In the presence of secondary flow, the velocity may be skewed towards the outer wall. Therefore, the hydrodynamic performance, viscous power loss and heat transfer can be affected significantly. The large pressure drop, enhanced mixing, and non-uniform wall shear stress are known as the major signatures of this type of flow. These make the curved channel flows differ significantly from those seen in the straight channels.

Since 1927, studies of curved flows in rectangular or circular channels have been numerous owing to its important role in fluid mechanics. One way to obtain the secondary flow insights that are experimentally impossible is to exploit computational fluid dynamics technique. This problem is particularly amenable to numerical simulation due to the relative ease of mesh generation. Besides the excellent paper reviewed by Berger *et al.* [6], we shall only cite few of the representative articles such as those by Patankar *et al.* [7], Humphrey [8], Soh and Berger [9], and Humphrey *et al.* [10] because space does not permit a full list of them. Studies of flow development in curved ducts with square cross-sections have been addressed on the determination of the critical Dean number, above which the formation-and-disintegration of secondary flow can lead to multiple-vortex-pair solutions [11, 12]. The effect of the channel curvature on the secondary flow development has also been the subject of considerable interest, in addition to the study of bifurcation phenomenon due to centrifugal instability [5, 13].

One way of exploring vortical flow in the currently investigated curved channel is to extract the physically meaningful insight from the enormous simulated velocity vector field. In this study, we employ the topological theory to exhibit three-dimensional flow separation and reattachment. By virtue of the simulated limiting streamlines [14] (or wall streamlines) or skin-friction lines [15], the kinematics of three-dimensional flow motion can be revealed. We also plot the density of helicity or its normalized value [16] to reveal the curved duct flow.

The rest of this paper is organized as follows. In the next section, the Navier–Stokes equations, subject to the divergence-free constraint condition and the well-posed boundary conditions, are solved using the in-house developed tri-quadratic Petrov–Galerkin finite element model [17]. The BiCGSTAB iterative solver [18] is used to overcome computational difficulties in association with the matrix indefiniteness and asymmetry. This is followed by describing the problem in Section 3 and the numerical results in Section 4. The evolving counter-rotating vortices are addressed in the result section. Finally, some conclusions are drawn in Section 5.

2. TRI-QUADRATIC STREAMLINE UPWIND FINITE ELEMENT MODEL

In this paper, the Navier–Stokes equations for incompressible fluid flows in the curved rectangular channels are solved under the laminar assumption. In dimensionless form, the conservation equations within the steady-state context are expressed in terms of the velocity vector $\underline{u}$ and the

pressure p:

$$\frac{\partial u_i}{\partial x_i} = 0 \tag{1}$$

$$\frac{\partial}{\partial x_m}(u_m u_i) = -\frac{\partial p}{\partial x_i} + \frac{1}{Re}\frac{\partial^2 u_i}{\partial x_m \partial x_m} \tag{2}$$

In the above, Re is denoted as the Reynolds number ($\equiv \rho u_{ref} L_{ref}/\mu$), where ρ is the density of the fluid flow. To close the above elliptic differential system, u_i should be prescribed on the entire boundary $\partial\Omega = \Gamma$.

Given that $\underline{w} \in H_0^1(\Omega) \times H_0^1(\Omega)$ and $q \in L_0^2(\Omega)$ in a simply connected domain Ω, the weak solutions for Equations (1)–(2) are solved subject to $\underline{u} = \underline{g}$ on $\partial\Omega$ from the following equations:

$$\int_\Omega (\underline{u} \cdot \nabla)\underline{u} \cdot \underline{w}\, d\Omega + \frac{1}{Re}\int_\Omega \nabla\underline{u} : \nabla\underline{w}\, d\Omega - \int_\Omega p\nabla \cdot \underline{w}\, d\Omega$$

$$= \int_{\Gamma/\Gamma_n} r\underline{w} \cdot \underline{n}\, d\Gamma + \int_{\Gamma/\Gamma_\gamma} \underline{s} \cdot \underline{w} \times \underline{n}\, d\Gamma \tag{3}$$

$$\int_\Omega (\nabla \cdot \underline{u})q\, d\Omega = 0 \tag{4}$$

In Equation (3), $\Gamma/\Gamma_{n,r}$ represents the complement of $\Gamma_{n,r}$ on $\Gamma = \partial\Omega$. If $\underline{\phi} \in \Gamma/\Gamma_i$ $(i = n, r)$ it, by definition, satisfies $\underline{\phi} \in \Gamma$ but $\underline{\phi} \notin \Gamma_i$. The unit vectors $\underline{n}$ and $\underline{s}$ are normal and tangent to Γ, respectively. The above weak formulation is closed by prescribing the following natural-type boundary conditions:

$$-p + \frac{1}{Re}\nabla\underline{u} \cdot \underline{n} = r \quad \text{on } \Gamma/\Gamma_n \tag{5}$$

$$\frac{1}{Re}\underline{n} \cdot \nabla\underline{u} \times \underline{n} = \underline{s} \quad \text{on } \Gamma/\Gamma_r \tag{6}$$

The appropriate finite element spaces for the chosen primitive variables are the key to success in obtaining the convergent finite element solutions from the mixed analysis of incompressible viscous fluid flows. For stability reasons, the shape functions chosen for $\underline{u}$ and p should satisfy the LBB (or inf–sup) condition [19, 20]. For this reason, we employ the tri-quadratic polynomials N^i $(i = 1 \sim 27)$ for $\underline{u}$ and use the tri-linear polynomials M^i $(i = 1 \sim 9)$ for p. Another key issue in simulating the high Reynolds number flow is to properly select the finite element test spaces to enhance the convective stability. The test function is constructed by adding a biased polynomial to the shape function. While the convective stability is enhanced, the resulting Petrov–Galerkin model may introduce considerable false diffusion errors in the multi-dimensional flow simulation. To avoid accuracy deterioration without sacrificing non-linear stability, it is essential to employ the weighting functions which can solely yield an artificial diffusivity along the streamline direction

[21]. Following this thought, $\tau\underline{u} \cdot \nabla N_i$ is added to the shape function N^i to render the weighting function given by $W_i = N_i + \tau\underline{u} \cdot \nabla N_i$, where the upwind coefficient τ is expressed as

$$\tau = \frac{\alpha_\xi V_\xi h_\xi + \alpha_\eta V_\eta h_\eta + \alpha_\zeta V_\zeta h_\zeta}{2V_j V_j} \tag{7}$$

In the above, $V_{y_i} \,(= \hat{e}_{y_i} \cdot \underline{u} \cdot \alpha_{y_i} = \frac{1}{2} V_{y_i} h_{y_i} Re\delta)$ is derived to obtain the nodally exact solution in the one-dimensional quadratic element [17], where δ is expressed in terms of $\gamma \,(\equiv V_{y_i} h_{y_i}/2\nu)$:

$$\delta(\gamma) = \begin{cases} \dfrac{1}{2} \cosh\left(\dfrac{\gamma}{2} - \dfrac{1}{\gamma}\right), & \text{at centre-nodes} \\[3mm] \dfrac{\cosh(\gamma) - 2}{\sinh(\gamma) - 4\tanh\left(\dfrac{\gamma}{2}\right)} - \dfrac{1}{\gamma}, & \text{at end-nodes} \end{cases} \tag{8}$$

The consequence of the resulting indefinite and asymmetric finite element matrix equations is the indispensable poor eigenvalue distribution. One can employ a Gaussian elimination direct solver to solve for the matrix equation. The storage requirement is, however, prohibitive for very large-size problems. For this reason, the Lanczos-type bi-conjugate gradient stabilized (BiCGSTAB) [18] iterative method will be employed in the present three-dimensional curved flow analysis. This approach is effective in the sense that it can locally minimize the residual through the generalized minimized residuals GMRES [22] and can avoid matrix transpose calculations. Nevertheless, the BiCGSTAB iterative solver still suffers from problems related to pivoting and Lanczos breakdowns. In order to reduce the matrix bandwidth, the matrix equations were element-by-element compressed [23].

3. PROBLEM DESCRIPTION AND CODE VALIDATION

In this study, we simulated the duct flow which was studied experimentally by Humphrey *et al*. [10]. The duct schematic in Figure 1 has a 90° bend with the mean radius of $R_c = 2.3$. The non-zero dimensionless length $\bar{\delta} \,(\equiv r_o/r_i = 1.556)$ can affect the balance of inertia, viscous, and centrifugal forces and, therefore, can play an ineglible role in the flow development. The elbow of 1×1 square cross-section has the downstream straight extension with a length 14 times the hydraulic diameter $D \,(= 1)$. It is, thus, rational to specify a fully developed flow at the truncated outlet plane EFGH. Since the deflected inlet vorticity may generate a strong transverse pressure gradient and, in turn, can affect the streamwise pressure gradient, a straight channel of a length 2 is attached upstream to the elbow. With U as the characteristic velocity (inflow velocity), D the characteristic length (duct hydraulic diameter) and μ the fluid viscosity, the channel flow will be investigated at $Re = 790$. In this benchmark exercise, the experimental condition of [10] was simulated. The fluid kinematic viscosity was $\nu = UD/Re$, with the bulk velocity magnitude of $U = 1$. The corresponding Dean number $De \,(\equiv Re(\frac{1}{2}d/R_c)^{1/2})$, which is another key parameter in the development of secondary flow, was 368.

We performed here the steady-state flow analysis in the full channel to model the Coanda effect [24]. The present calculations were performed in a non-uniformly discretized domain, with 201 grid points distributed in the streamwise direction and 41×41 grid points at each (y, z) cross-section. The simulated solutions at 337 881 nodal points have been shown to be capable of resolving the secondary flow according to the grid-independence test.
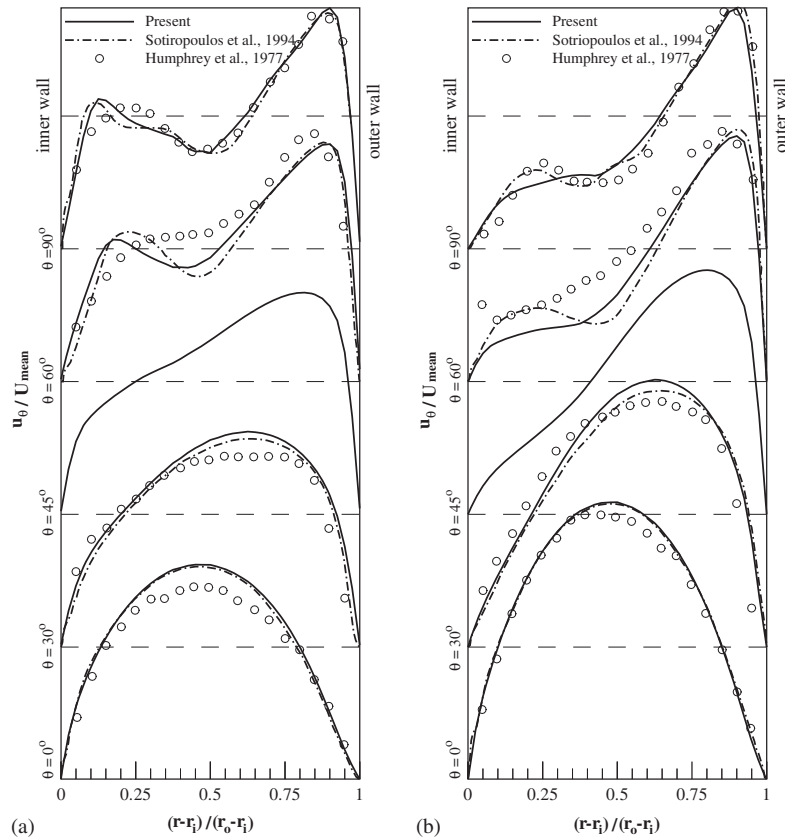
Figure 1. Schematic of the investigated curved duct.

To confirm the validity of the present finite element calculation, we have compared the simulated solutions with both the experimental [10] and numerical [25] data for the streamwise velocity $u_\theta(r)$ obtained in the curved sections at two planes $y = 0.25$ and 0.5. In Figure 2 good agreement is seen except at planes near $\theta = 60°$. The reason for the discrepancy between the experimental and predicted results remains unclear. Comparison of axial velocities in the radial direction was also carried out at different angles θ. As Figure 3 shows, the agreement between the numerical solutions is better than that between the numerical and experimental data except at $\theta = 60°$.

Figure 2. Comparison of the simulated velocity profiles $u_\theta(r, y)$ with other two solutions obtained at different angles θ defined in Figure 1: (a) $y = 0.25$ plane; and (b) $y = 0.5$ plane.

4. NUMERICAL RESULTS

Near the inner bend, the axial flow seen in Figure 2 undergoes a rapid decrease in velocity and is seen to form a step-like profile. Farther downstream, the continuously eroded step-like axial velocity forms a new local maximum near the inner bend. In between the two local peaks, a deep valley is, thus, seen. This valley remains deep up to the plane near $\theta = 90°$. Afterwards, a continuous flatting is observed in the direction towards the exit plane. The axial velocity profile manifested by the local maxima and the valley present in between was experimentally confirmed by Humphrey *et al.* [10] in the curved channels. The step-like axial velocity profile present near the inner bend was also experimentally reported by [26] and numerically simulated by Soh and Berger [9] for a circular pipe.

4.1. Curved flow feature and topology

The entry flow plotted in Figure 4 is characterized by the boundary layer type, with the peak axial velocity found on the plane of symmetry. Upstream of the curved duct, the flow is accelerated in
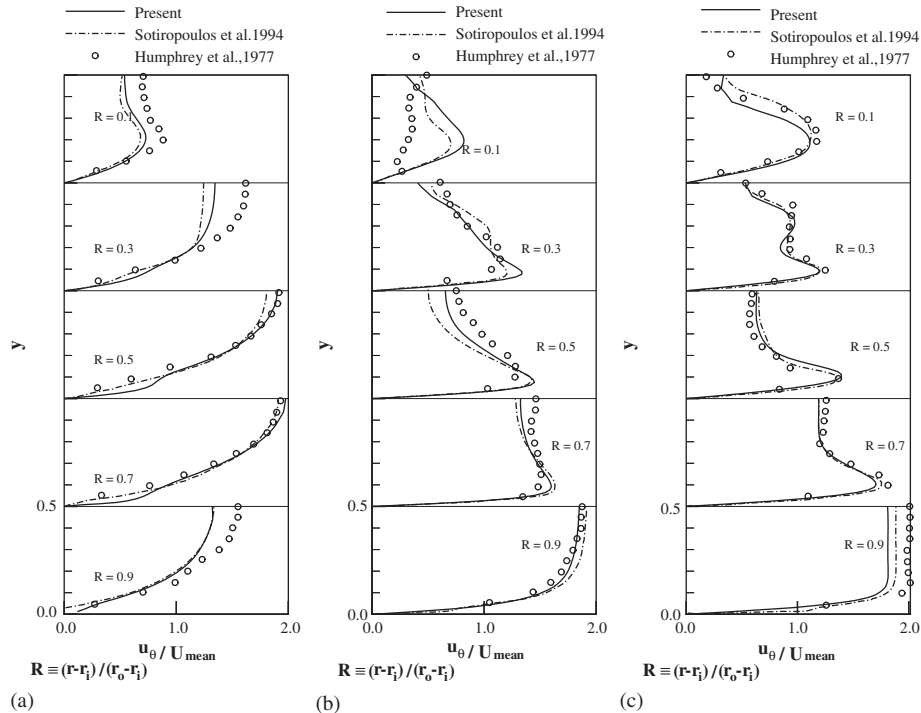
Figure 3. Comparison of the simulated $u_\theta(r, y)$ against r with other two solutions obtained at different angles θ defined in Figure 1: (a) $\theta = 30°$; (b) $\theta = 60°$; and (c) $\theta = 90°$.

regions near the inner-radius wall due to the favourable longitudinal pressure gradient. Conversely, the decelerated flow is observed in regions near the outer-radius wall because of the developed adverse pressure gradient downstream of $0°$. The peak axial velocity is shifted towards the outer wall owing to the centrifugal effect. The degree of velocity skewness increases with the increasing turning angle. Such a skewed axial velocity can persist far downstream. The outer bend is referred to as the pressure side and the inner bend as the suction side. The evidence is given in Figure 5, which plots the pressure coefficient C_p along the inner- and outer-radius walls in the vicinity of the symmetry plane. The difference in C_p at the inner and outer walls is gradually diminished at a location downstream of the $90°$ plane. The pressure obtained at the inner bend is seen to decrease gradually and monotonically with θ. The dramatic pressure rise along the outer bend results in the aforementioned adverse pressure gradient in the region close to the entry plane. Such an adverse pressure gradient developed along the outer bend may cause the streamwise separation to occur. The longitudinal recirculation, while being weak in vortex strength and small in eddy size, has been experimentally observed [10].

In Figure 6, $p(r)$ at $y = 0$, 0.25 and 0.5 planes are plotted to show the presence of inwardly directed radial pressure gradient in the bend. The force imbalance between this inwardly directed radial pressure gradient and the centrifugal force causes the secondary flow to develop at the cross-section planes. The fluid in the core region is seen to move towards the outer wall and return to the inner wall along the channel wall, thereby resulting in a vortex. In the present full
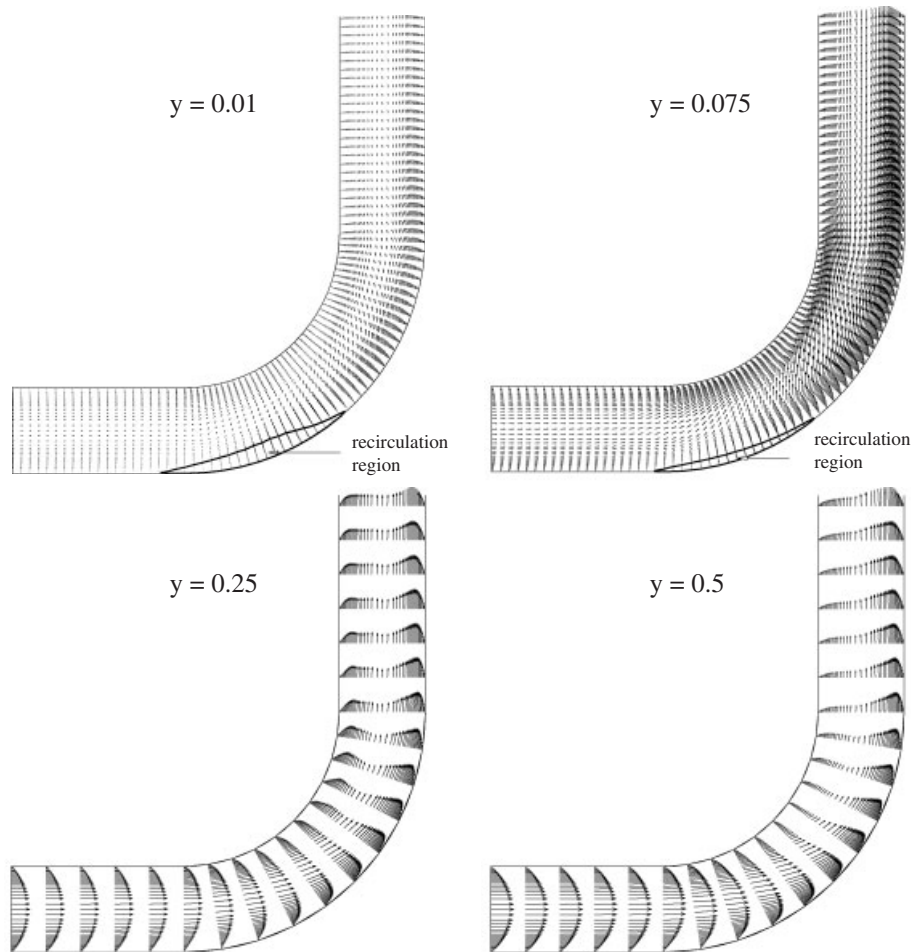
Figure 4. The simulated velocity vectors at different *y*-planes.

channel simulation, the simulated secondary flow has two counter-rotating vortices at the channel cross-section for $0° \leqslant \theta \leqslant 40°$. Two vortices are symmetric with respect to the plane of symmetry. The axial flow superimposed over the secondary flow makes the flow pattern a substantially three-dimensional type in the curved section, as schematically shown in Figures 7 and 8. To assert that flow separation from the outer wall indeed exists, we plot the three-dimensional separation regions in Figure 7. Immediately adjacent to the two end walls, there exist some regions of streamwise flow separation. Along the direction towards the inner wall, the separated flow increasingly reduces its size and finally shows no separation near the plane of symmetry. The presence of outer-bend separated flows near the two end walls indicates the necessity of conducting the current three-dimensional flow analysis in the curved duct.
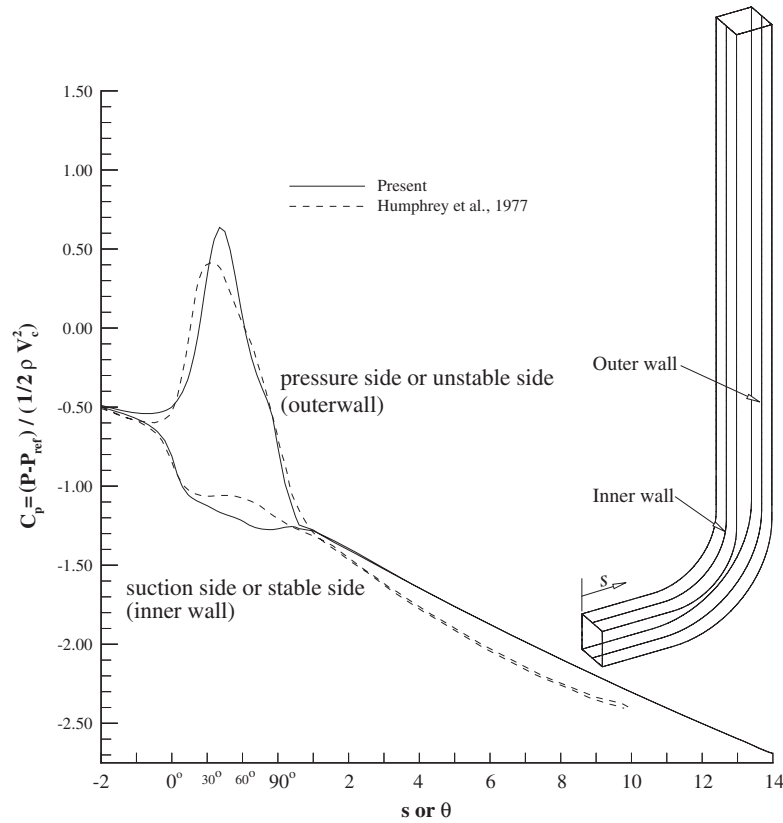
Figure 5. Comparison of the pressure distributions for $p(s, \theta)$ along the inner and outer walls at the plane of symmetry. Here, θ is defined in Figure 1.
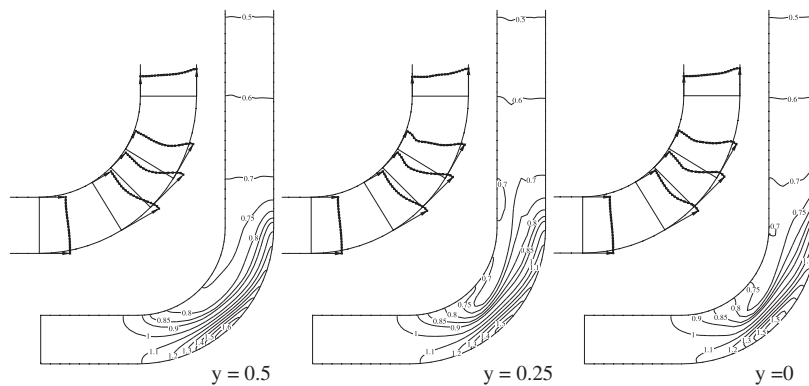

Figure 6. The simulated pressure contours at three chosen y-planes:
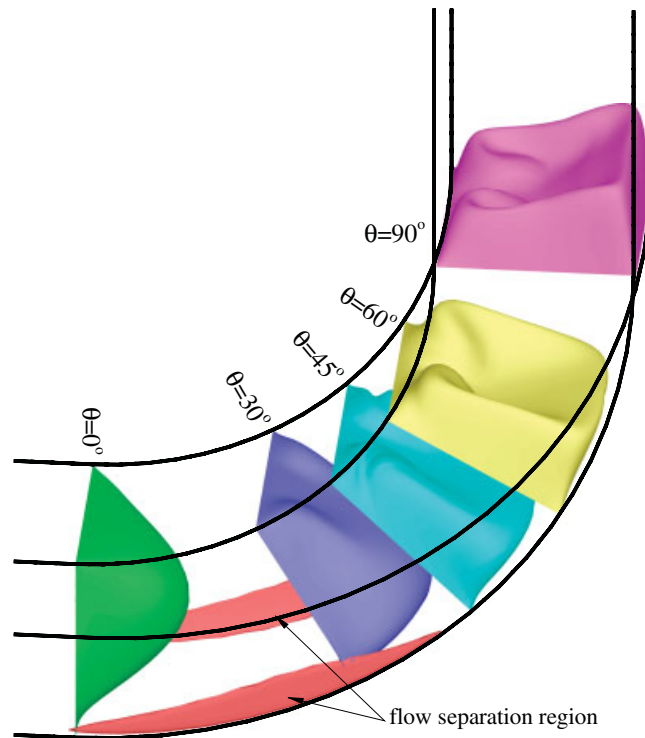(a) $y = 0.5$; (b) $y = 0.25$; and (c) $y = 0$.

Figure 7. The simulated three-dimensional velocity magnitude contours at the five chosen curved sections for showing the separation region.

Figure 9 plots the streamlines at several chosen cross-sections. The number of vortex pairs is seen to increase from one to two and then three. Each vortex direction is opposed to its adjacent one. This physically rational bifurcation phenomenon was firstly predicted by Akiyama [27] and then experimentally confirmed by Joseph *et al.* [28] in the curved channels as the Dean number is larger than 100 [29]. According to Ghia and Sokhey [30], the increased number of vortex pairs at the cross-flow planes is attributable to the centrifugal instability. As Figure 9 shows, weak vortex is present in the corner of the inner and end walls. The primary counter-rotating vortex is gradually distorted with the vanishing corner vortex near the end wall. This is accompanied by another vortex forming at the inner bend near the plane of symmetry. Farther downstream, this vortex is strengthened by the primary vortex that has been increasingly distorted and elongated. At about $\theta = 66°$, the primary vortex becomes distorted and it can be divided into two large corotating vortices. In between the two vortices of different rotation signs, a topological saddle point is present. The tendency of dividing the primary vortex into two vortices is deemed to be responsible for the step-like axial velocity profile [12]. The increased number of vortex pairs is accompanied by the decreased vorticity strength. This finding is logical since the flow will be fully developed again at the exit plane.

Due to the formation of secondary flow and the presence of skewed axial velocity, the wall shear varies circumferentially, with the maximum and minimum helicity magnitudes found, respectively,
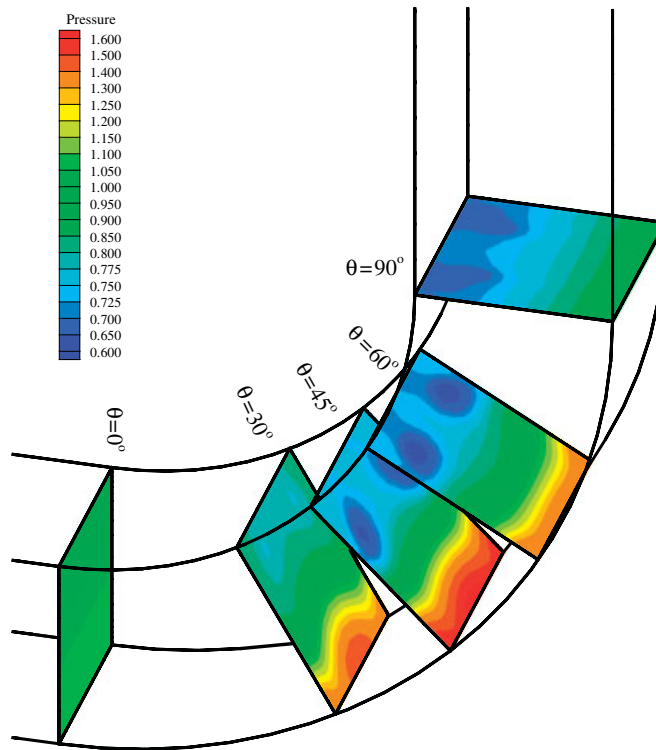
Figure 8. The simulated three-dimensional pressure contours at the five chosen curved sections.

at the outer and the inner walls of the bend. To confirm this, we plot in Figure 10 the wall shear stresses at the inner and outer walls. It is found that the simulated shear stress contours at the outer bend are far more complicated than those plotted at the inner bend, with the observed oscillatory shear stress. An explanation for such stress pattern found near the outer bend is due to the fluid flowing over the concave wall. This tends to destabilize the curved flow. The degree of instability increases with the increasing larger Reynolds number. Under the circumstances, the Taylor–Görtler vortices may be developed in the flow.

Amongst the vector fields that can be chosen in the topological study of three-dimensional flow field, we employed the limiting streamlines, which are known to be the streamlines present immediately above the channel wall [14]. By plotting the topologically singular points, the simulated nodes, foci, and saddles on each curved channel wall in Figure 9 can help us to understand the kinematic nature of the investigated flow based on the topological rule of Davey [31] and Lighthill [15]. In Figure 11, it is seen that the simulated limiting streamlines are directed either towards or away from the topological singular point. The lines of separation are found to originate from the saddle point and will terminate either at a spiral node in the flow interior or at the half-node at the intersection line of two adjacent walls. Unlike the lines of separation, the wall-streamlines adjacent to the line of reattachment are seen to be repelled from this singular line. We also plot in Figure 11 reattachment lines, which emanate from the node and terminate at the
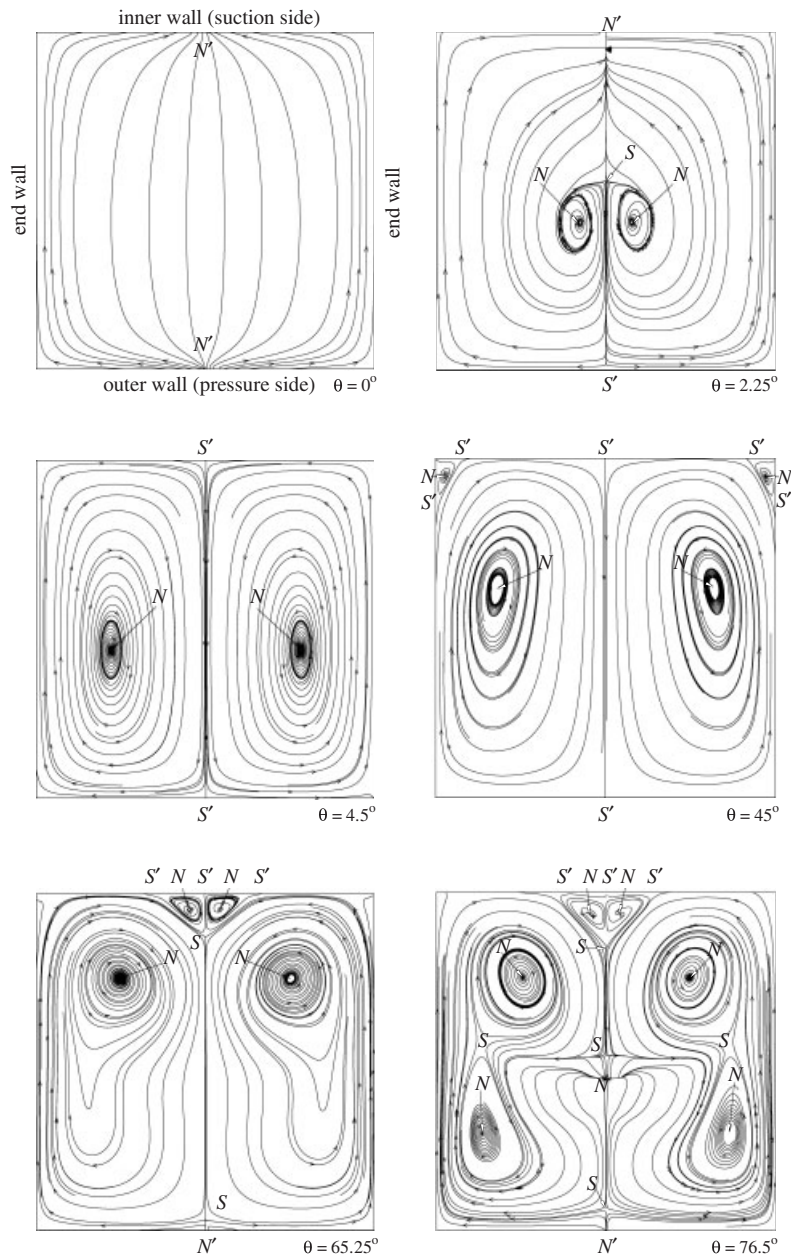
Figure 9. The simulated streamlines at different θ-planes. The topological points are labelled for showing that the predicted solutions satisfy the topological rule $(N - S) + \frac{1}{2}(N' - S') = 1$. Here, N, S, N' and S' denote the node, saddle, half-node and half-saddle, respectively.
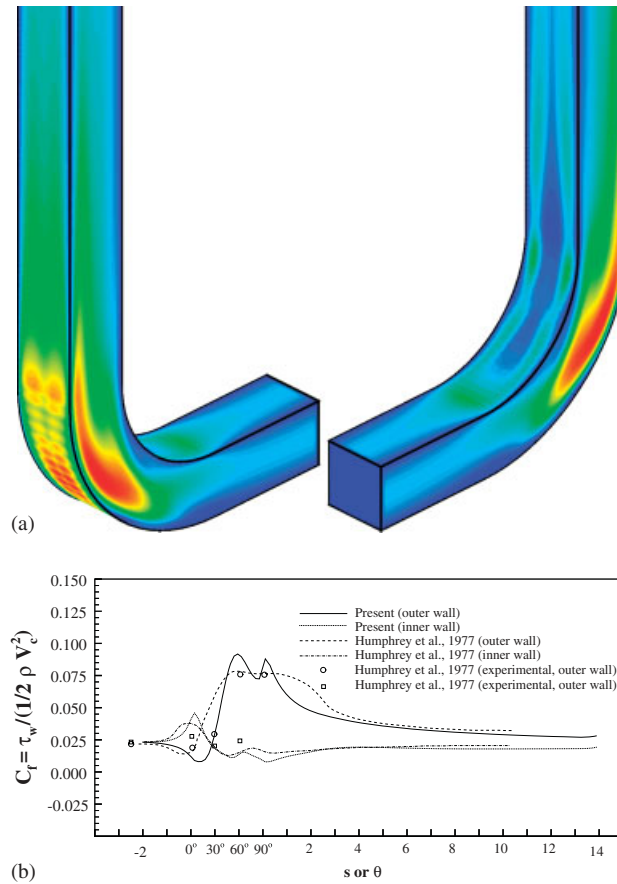
Figure 10. (a) The simulated wall shear stress contours; and (b) the simulated wall shear stresses along the inner and outer walls of the channel at the plane of symmetry $y = 0.5$.

saddle. The simulated reattachment lines have two nodes, in between two topological nodes, there is a half-node located exactly at the intersection of two planes.

4.2. Vortex stability

Although the investigated problem is simple in geometry, the flow complexity is much beyond our expectation. Especially noteworthy is the formation of spiralling flow. To get additional insight into the vortical flow development in the curved duct, we plot the vortical coreline, which is regarded as the global signature of the associated vortical flow. By definition, all three-dimensional foci span the vortical coreline. The velocity components orthogonal to the vortical coreline are zero at the spiral focal point. By virtue of this definition, we can plot the vortical coreline in Figure 12. Hereafter, we refer to u_s as the velocity component tangential to the vortical coreline. In light of the non-zero u_s, we were led to realize that the fluid particles near the vortical coreline will
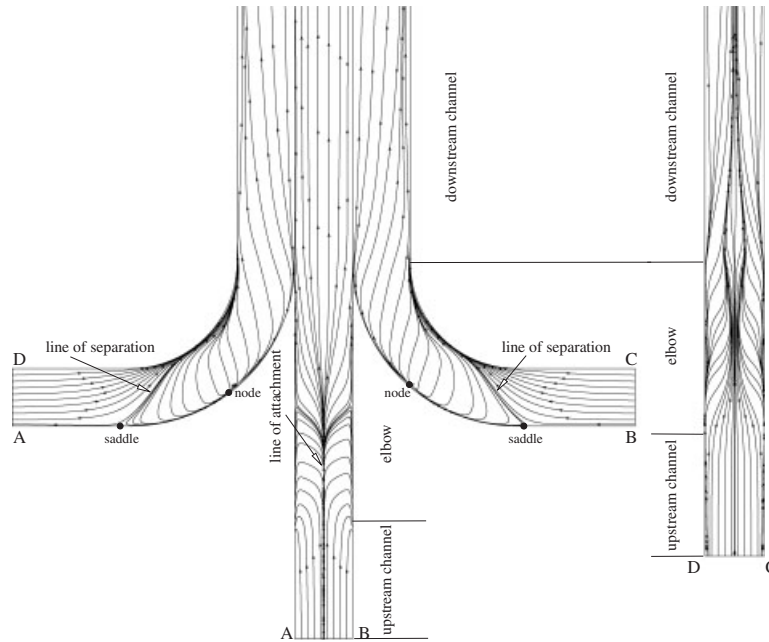
Figure 11. The simulated limiting streamlines at each no-slip wall.

continue their spiral journey downwards. To confirm this, the massless markers were seeded near each vertical end wall so as to enable us to trace their trajectories.

In this paper, we also plot in Figure 13 the value of $\lambda \equiv (\partial u_s/\partial s)$, where s denotes the unit tangent vector to the vortical coreline. Since $u_{t_1}|_0 = u_{t_2}|_0 = 0$ along the vortical coreline passing through '$\circ$', schematic in Figure 14, the equation of motion along this line can be simplified as

$$\triangle = \frac{1}{\rho u_s|_0} \left[\frac{\partial p}{\partial s}\bigg|_0 - \mu \left(\frac{\partial^2 u_s}{\partial t_1^2} + \frac{\partial^2 u_s}{\partial t_2^2} + \frac{\partial^2 u_s}{\partial s^2} \right) \right]$$

where $\triangle$ represents the divergence of the simulated velocity components. In the case of high Reynolds numbers (or in the case of negligibly small μ), the sign of $\triangle$ varies depending on the value of u_n and on the pressure gradient $\partial p/\partial s$ evaluated at the nodal point '$\circ$'. Simple algebra shows that if $u_s|_0 > 0$ and $\partial p/\partial s|_0 < 0$, then $\triangle < 0$ (or $\lambda > 0$), thereby resulting in an accelerating flow (Figure 13). Otherwise, if $u_s|_0 > 0$ and $\partial p/\partial s|_0 > 0$, then we have $\triangle > 0$ (or $\lambda < 0$). Under the circumstance, the flow is of the deceleration type (Figure 13). For completeness, we also plot in Figure 13 the normalized helicity $\Phi (\equiv \underline{u} \cdot \underline{\omega}/|\underline{u}||\underline{\omega}|)$ along the vortical coreline for showing the intensity of the simulated spiralling flow motion.

The secondary flow inside the rectangular curved channel is deemed to be responsible for the change of sign in λ. At the upstream side, λ is seen to have the negative value. The streamline at the transverse planes, which are located upstream of $\lambda = 0$, repels from the spiral node and the streamwise flow is of the decelerated type. Immediately downstream of $\lambda = 0$, the simulated cross-flow start to show two families of spiralling flow to respond the presence of positive λ. The flow at the outer part spirals towards the vortical coreline and the flow at the inner part repels
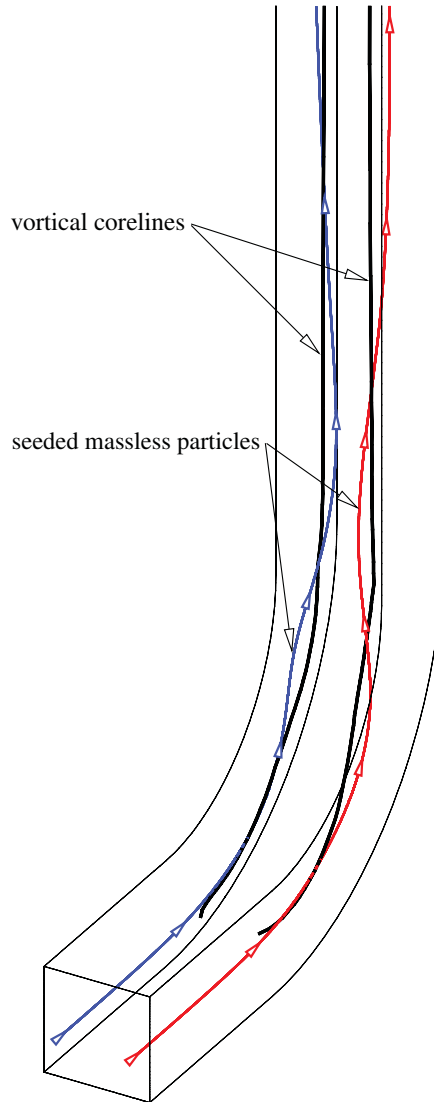
Figure 12. The simulated three-dimensional vortical corelines and the surrounding
spiralling particle trajectories.

spirally from 'o'. Both of them, however, proceed downstream in a clockwise direction. This inward-and-outward motion results in a ring (or limiting cycle) in the sense that the fluid particles within the ring cannot spiral towards the vortical core. On the other hand, fluid particles outside of the ring cannot spiral outwards.

In view of the limiting cycles on the cross-flow planes, it is instructive to reveal the subtle changes in vortex motion in the vicinity of $\lambda = 0$. In Figure 15, the inward spiralling flow region is seen to decrease in size. The flow, as a result, becomes unstable as it proceeds downwards. This is
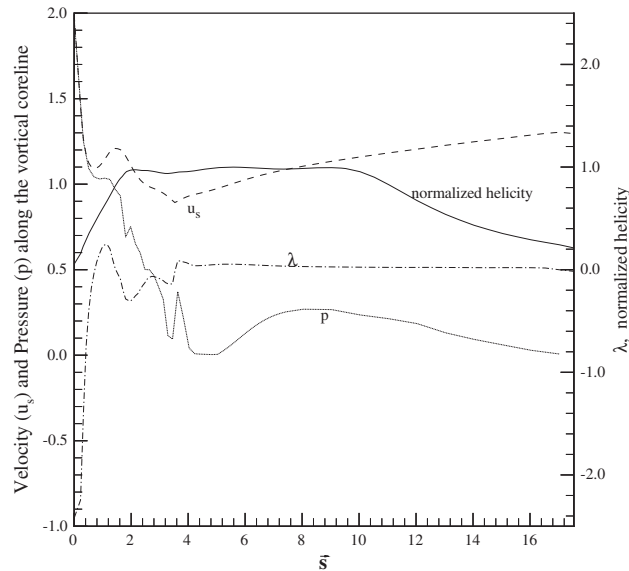
Figure 13. The simulated velocity component u_s, pressure p, normalized helicity and helicity gradient $\lambda (\equiv \partial u_s/\partial s)$ along the vortical coreline having the unit vector s.
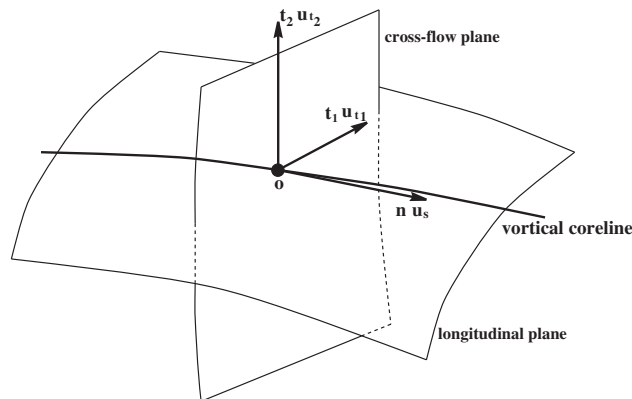

Figure 14. Illustration of the plane which is locally orthogonal to a vortical coreline. The longitudinal plane is also plotted.

followed by the decreasing value of λ. The presence of unstable limiting cycle indicates the possible onset of Hopf bifurcation. Under these circumstances, flow unsteadiness may become increasingly pronounced in the subsequent flow development. The limiting cycle is seen again as λ becomes negative. As the limiting cycles appear, circles which are stable or unstable alternately show their presence. It is impossible to find two consecutive cross-flow planes, in which the limiting cycles are either stable or unstable [32]. Therefore, a vortex can be destabilized under the conditions of $\partial u_s/\partial s < 0$ and $u_s \geqslant 0$ along the vortical coreline.
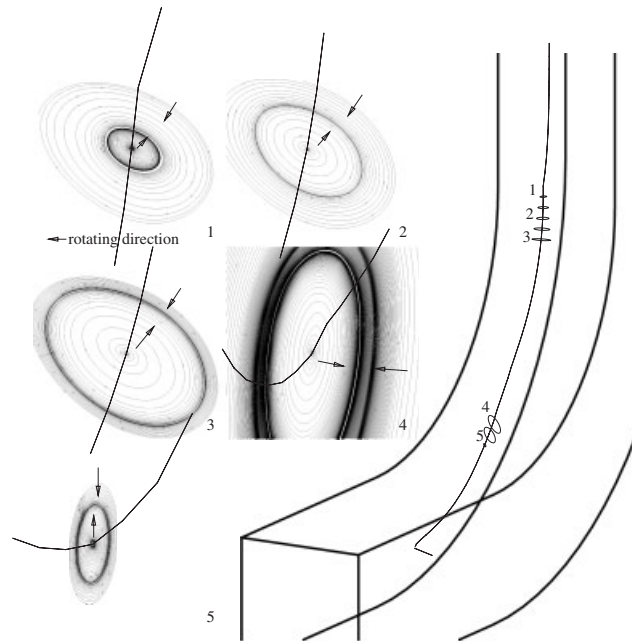
Figure 15. The simulated streamlines at the planes that are locally normal to the vortical coreline.

5. CONCLUDING REMARKS

In this study, the three-dimensional steady-state Navier–Stokes equations, subject to the incompressibility constraint condition, are solved by employing the streamline upwind finite element model so as to enhance convective stability and to mininize the false diffusion error. To resolve the asymmetry and indefiniteness problems in the large-size finite element matrix equations, we have applied the element-by-element BiCGSTAB iterative solver for improving the convergent performance. At a streamwise plane that is upstream of the bend with a length of 2, the location with the peak axial velocity at the plane of symmetry shifts towards the outer wall owing to the centrifugal force. The skewed axial flow rapidly intensifies up to about $\theta = 30°$. This progressively developing flow is accompanied by an acceleration flow in regions near the inner-radial wall. In the bend between the 0 and 40° streamwise planes, the fluid flows near the outer wall are seen to be greatly decelerated due to the adverse longitudinal pressure gradient. Conversely, the favourable pressure gradient observed at the suction side of the bend can cause the flow to accelerate. This acceleration can be further strengthened by the high-speed fluid transferred by the secondary flow motion proceeding from the duct centre towards the outer-radius wall. Such a pronounced profile is clearly observed at the downstream station. The simulated secondary flow is characterized by having the fluid particles moving towards the side wall along the outer-radius (pressure) wall and the symmetry plane along the inner-radius (suction) wall. In the simulated curved channel, the streamlines at cross-sections are seen to spiral towards and away from the vortical coreline as $\lambda\,(\equiv \partial u_s/\partial s)$ changes sign. The limiting cycle develops as a consequence of the inward-and-outward particle motion. These evolving limiting cycles have different sizes and

can be classified as stable or unstable, depending on the sign of $\partial u_s / \partial s$. The simulated limiting cycles are stable when λ is evolved from the positive value to the negative value. In contrast to the stable limiting cycle, the cycle is unstable if λ changes its sign from the negative to positive. Once the limiting cycles appear, circles which are stable or unstable will alternately show their presence. When $\partial u_s / \partial s < 0$ and $u_s > 0$, it is highly possible that the vortical flow becomes stable.

ACKNOWLEDGEMENTS

REFERENCES

1. Bennett J, Hall P, Smith FT. The strong nonlinear interaction of Tollmien–Schlichting waves and Taylor–Görtler vortices in curved channel flow. *Journal of Fluid Mechanics* 1991; **223**:475–495.
2. Eustice J. Flow of water in curved pipes. *Proceedings of the Royal Society of London, Series A* 1910; **84**:107–118.
3. Eustice J. Experiments on stream-line motion in curved pipes. *Proceedings of the Royal Society of London, Series A* 1911; **85**:119–131.
4. Dean WR. Note on the motion of fluid in a curved pipe. *Philosophical Magazine* 1927; **20**:208–223.
5. Dean WR. The stream-line motion of fluid in a curved pipe. *Philosophical Magazine* 1928; **30**:673–693.
6. Berger SA, Talbot L, Yao LS. Flow in curved pipes. *Annual Review of Fluid Mechanics* 1983; **15**:461–512.
7. Patankar SV, Pratap VS, Spalding DB. Prediction of laminar flow and heat transfer in helically coiled pipes. *Journal of Fluid Mechanics* 1974; **62**:539–551.
8. Humphrey JAC. Flow in duct with curvature and roughness. *Ph.D. Thesis*, Imperial College of Science and Technology, London, U.K., 1977.
9. Soh WY, Berger SA. Laminar entrance flow in a curved pipe. *Journal of Fluid Mechanics* 1984; **148**:109–135.
10. Humphrey JAC, Taylor AMK, Whitelaw JH. Laminar flow in a square duct of strong curvature. *Journal of Fluid Mechanics* 1977; **83**:509–527.
11. Bara B, Nandakumar K, Masliyah JH. An experimental and numerical study of the Dean problem: flow development towards two-dimensional multiple solutions. *Journal of Fluid Mechanics* 1992; **244**:339–376.
12. Soh WY. Developing fluid flow in a curved duct of square cross-section and its fully developed dual solutions. *Journal of Fluid Mechanics* 1988; **188**:337–361.
13. Winters KH. A bifurcation study of laminar flow in a curved tube of rectangular cross-section. *Journal of Fluid Mechanics* 1987; **180**:343–369.
14. Legendre R. Séparation de courant léconlment laminaire tridimensional. *Recherche Aérospatiale* 1956; **54**:3–8.
15. Lighthill MJ. Attachment and separation in three-dimensional flow. In *Laminar Boundary Layers*, vol. 2.6, Rosenhead L (ed.). Oxford University Press: Oxford, 1963; 72–82.
16. Levy Y, Degani D, Seginer A. Graphical visualization of vortical flows by means of helicity. *AIAA Journal* 1990; **28**(8):1347–1352.
17. Sheu WH, Wang MT, Tsai SF. Element by element parallel computation of incompressible Navier–Stokes equations in three dimensions. *SIAM Journal on Scientific Computing* 2000; **21**(4):1387–1400.
18. Van der Vorst HA. BI-CGSTAB: a fast and smoothly converging variant of BI-CG for the solution of nonsymmetric linear systems. *SIAM Journal on Scientific and Statistical Computing* 1992; **13**(2):631–644.
19. Babuška I. Error bounds for finite element methods. *Numerische Mathematik* 1971; **16**:322–333.
20. Brezzi F, Douglas J. Stabilized mixed methods for the Stokes problem. *Numerische Mathematik* 1988; **53**:225–235.
21. Hughes TJR. *Finite Element Methods for Convection Dominated Flows*, AMD, vol. 34. ASME: New York, 1979.
22. Saad Y, Schultz MH. GMRES: a generalized minimum residual algorithm for solving nonsymmetric linear system. *SIAM Journal on Scientific and Statistical Computing* 1986; **7**:856–869.
23. Wang MT, Sheu WH. An element-by-element BiCGSTAB iterative method for three-dimensional steady Navier–Stokes equations. *Journal of Computational and Applied Mathematics* 1997; **79**:147–165.
24. Wille R, Fernholz H. Report on the first European Mechanics Colloquium, on the Coanda effect. *Journal of Fluid Mechanics* 1965; **23**(4):801–819.

25. Sotiropoulos F, Kim WJ, Patel VC. A computational comparison of two incompressible Navier–Stokes solvers in three-dimensional laminar flows. *Computers and Fluids* 1994; **23**(4):627–646.
26. Agrawal Y, Talbot L, Gong K. Laser anemoneter study of flow development in curved circular pipes. *Journal of Fluid Mechanics* 1978; **85**:497–518.
27. Akiyama M. Laminar forced convection heat transfer in curved rectangular channels. *Ph.D. Thesis*, Department of Mechanical Engineering, University of Alberta, Canada, 1969.
28. Joseph B, Smith EP, Adler RJ. Numerical treatment of laminar flow in helically coiled tubes of square cross-section. *AIChE Journal* 1975; **21**:965–974.
29. Jayanti S, Hewitt GF. A numerical study of bifurcation in laminar flow in curved ducts. *International Journal for Numerical Methods in Fluids* 1992; **14**:253–266.
30. Ghia KN, Sokhey JS. Laminar incompressible viscous flow in curved ducts of rectangular. *Journal of Fluids Engineering* 1977; **99**:644–648.
31. Davey A. Boundary-layer flow at a saddle point of attachment. *Journal of Fluid Mechanics* 1961; **10**:593–610.
32. Zhang H. Bifurcation of vortex motion along its axis. *ACTA Aerodynamica Sinica* 1994; **12**(3):243–251.